Applied Surface Science 254 (2008) 5445–5451

Contents lists available at ScienceDirect

Applied Surface Science

journal homepage: www.elsevier.com/locate/apsusc

Chemisorption of hydrogen sulphide on zinc oxide modified aluminum-substituted SBA-15

Xiaohui Wang, Jinping Jia, Ling Zhao, Tonghua Sun *

School of Environmental Science and Engineering, Shanghai Jiao Tong University, 800 Dongchuan Road, Shanghai 200240, PR China

ARTICLE INFO

Article history:
Received 11 January 2008
Received in revised form 19 February 2008
Accepted 22 February 2008
Available online 29 February 2008

PACS:
81.05.Rm
81.07.Wx
82.33.Ln

Keywords:
Adsorption
Hydrogen sulphide
Mesostructure
Desulphurization
Zinc oxide nanostructure

ABSTRACT

Aluminum silicate mesoporous material, ZnO/Al–SBA-15, was synthesized by post-synthesis and immobilization method via microwave-assisted route. Desulphurization tests from a gas mixture with low content H_2S were carried out as the probing reaction on these materials. Chemical effects and the nature of the ZnO additive and textural properties on desulphurization capacity were studied over this material. Material was characterized using N_2 adsorption, XRD, TEM, FTIR, XPS, ICP and other techniques. The analysis suggests that the as-synthesized material had well-ordered hexagonal mesopores and was abundant in micropores. ZnO nanoparticles dispersed well and anchored both in the channel and the wall of mesoporous silica. The material with 2.1 wt.% zinc loading presented the highest H_2S uptake capacity. Both micropores and mesopores are active sites for H_2S capture, especially micropores. The enhancement of H_2S removal capacity was attributed to the integration of the pore structure of mesoporous material and the promising desulphurization properties of ZnO nanoparticles. ZnO/Al–SBA-15 could be an effective alternative to remove H_2S from gaseous streams and it also extends the research of mesoporous material.

1. Introduction

The narrow and uniform pore size of mesoporous materials with extremely high surface area holds much promise for the development of novel solid catalysts since 1992 [1]. Many inherent properties make SBA-15-related materials among the best candidates for applications in catalysis [2–4], sorption [5], separation [6,7], sensor design [8] and nanoscience [9–15]. SBA-15 has thicker pore walls, wider pore sizes, higher thermal and hydrothermal stability than other silicate mesoporous materials [16]. It is characterized by having the wide pore openings and mesopores which is interconnected by micropores across the silica walls [17]. Furthermore, the amount of these micropores is considerable. Micropore may endow such materials with exciting properties in sorption, catalysis, etc. The open mesoporous structure provides highly dispersed and spatially uniform active sites. Inclusion of well-defined catalytic phases drastically changes the microenvironment inside the mesopores. It was therefore of interest to introduce additional catalytic functions by incorporation of active sites in the silica walls or by deposition of active species on the inner surface of the material, which can yield improved hydrothermal stability and catalytic activity. However, the formation of isolated or at least highly dispersed active centers on the surface of mesoporous materials is less straightforward because the amorphous framework only exhibits low ion-exchange capacity [18].

In this study, many strategies such as substitution of elements in the framework and immobilization of active species with predetermined structure were used for the design and the preparation of mesoporous catalysts. In addition, microwave-assisted preparation method was used to scatter guests homogeneously into host pores. Mixed mesoporous silica containing heteroatom Al incorporated into the silica for further immobilizing catalytic active species was synthesized.

The removal of sulphur-containing species is currently a strategic issue [19]. Hydrogen sulphide gas occurs naturally in crude petroleum, natural gas, volcanic gases and hot springs. It also can result from industrial activities, such as food processing, coke ovens, kraft paper mills, tanneries and petroleum refineries. Many industrial processes, such as the Claus process and natural gas sweetening, are characterized by H_2S streams at relatively low temperatures [20]. Consequently a desulphurization test from a

* Corresponding author. Tel.: +86 21 54749910; fax: +86 21 54749910.
E-mail address: sunth2007@163.com (T. Sun).

0169-4332/$ – see front matter © 2008 Elsevier B.V. All rights reserved.
doi:10.1016/j.apsusc.2008.02.086

gas mixture containing low content H_2S was selected as probing reaction on these materials. Among adsorbents for H_2S removal at low temperature, zinc oxide (ZnO) has a very high equilibrium constant, removing H_2S down to fractions of 1 ppm. Therefore, ZnO nanoparticle was chosen as the active species.

The main objective of this study is to elucidate the feasibility and potential of using Al–SBA-15 supported nano-scale ZnO as an adsorbent for H_2S removal from gaseous streams at ambient conditions. The characterizations of materials before and after desulphurization experiments were carried out by ICP, N_2 adsorption, XRD, FTIR, TEM and XPS analysis to obtain more information in the development of new adsorbents. The results showed that the as-synthesized material has conspicuous promise for H_2S capture at ambient conditions.

2. Materials and methods

2.1. Materials

2.1.1. Synthesis of SBA-15

Twenty grams of poly (ethylene glycol)-block-poly (propylene glycol)-block-poly (ethylene glycol) ($EO_{20}PO_{70}EO_{20}$, Aldrich) was dissolved in 495 ml of water and 2 M HCl solution 37 ml while stirring, then 45 ml of tetraethyl orthosilicate (TEOS) was added. The obtained suspension was stirred at 313 K for 24 h and then at 373 K for 20 h. The solid product was filtered, washed, dried in air and finally calcined at 823 K for 5 h. The white powder obtained, SBA-15 silica, is designated as S.

2.1.2. Synthesis of Al–SBA-15

Anhydrous aluminum chloride (3.7 g) was dissolved in 250 ml absolute alcohol, followed by the addition of 7.5 g SBA-15. The mixture was stirred for 12 h at room temperature, then filtrated, washed with absolute alcohol, dried in air, and finally calcined at 823 K for 5 h. Al–SBA-15 is denoted as AS.

2.1.3. Synthesis of Al–SBA-15 supported ZnO

Three hundred milliliter of 2 M sodium carbonate was added in 200 ml of 2 M zinc nitrate while stirring. The mixture was then washed with 200 ml of 0.1 M ammonia and 100 ml of absolute ethanol, dried at 393 K for 15 h, and finally calcined in air at 523 K for 1.5 h. The white powder obtained was ZnO nanoparticle. Ration ZnO was mixed with 1.0 g of Al–SBA-15 in an agate mortar for 20 min. The mixture was then treated in a microwave oven (WP800SL23-2, Galanz, China) for 20 min. The samples are denoted as ASZ-1–5 which mean different Zn content.

2.2. Desulphurization test

The desulphurization test was carried out to evaluate the H_2S removal capacity over the as-synthesized material. A given amount of material was packed into a U-type glass column (length of 350 mm, diameter of 8 mm). Five hundred milliliters per minute of a gas mixture (containing 0.1% H_2S, balance of air) passed through the reactor. The gas flow rates were controlled by a mass flow controller system (FMA-700 series controllers coupled with an FMA-78P4 readout/power supply, Omega). The inlet and outlet gas was analyzed by gas chromatograph (Shimadzu, GC2010) equipped with a flame photometry detector (FPD). All outlet gases from the reactor were sampled with an online auto-sampling system and analyzed every minute. The test was terminated when the outlet concentration was 50 ppm. The breakthrough time was defined as the time from the beginning of desulphurization process to the time when the H_2S concentration at the outlet reached 0.1 ppm. The H_2S breakthrough capacity expressed in milligrams of sulphur per gram of material was calculated by the integration of the area above the breakthrough curve and from H_2S concentration in the inlet gas, flow rate, breakthrough time, and the mass of material. The scheme was presented in Fig. 1. The exhausted samples after desulphurization test are designated with the additional letter "E."

2.3. Characterization

Dry material (0.4 g) was added to 20 ml of deionized water, stirred overnight and filtered. The pH value of the solution was measured using an Accumet Basic pH meter (Fisher Scientific, Springfield, NJ). Elemental compositions of samples were studied with Inductive Coupled Plasma (IRIS ADVANTAGE/1000, TJA Corporation, USA). The structural characteristics of samples were determined by Fourier Transform Infrared Spectrophotometer (EQUINOX 55, BRUKER, Germany) (400–4000 cm^{-1}). X-ray diffraction (XRD) patterns were obtained with an X-ray diffractometer (D8Advance, BRUKER, USA; Cu Kα radiation, λ = 1.5406 Å). The surface morphology was performed on a Transmission Electron Microscope (JEM-2100F, JEOL, Japan), operating at an acceleration voltage of 200 kV. The isotherms of nitrogen adsorption–desorption were performed at 77 K using a Gas Absorption Analyzer (TriStar 3000, Micromeritics, USA). The Brunauer–Emmett–Teller (BET)-specific surface area was evaluated using adsorption data. The micropore surface area and micropore volume were determined by the *t*-plot method. The Barrett–Joyner–Halenda (BJH) model [21] was used to determine the pore size distributions from the desorption portion of the isotherm [22].

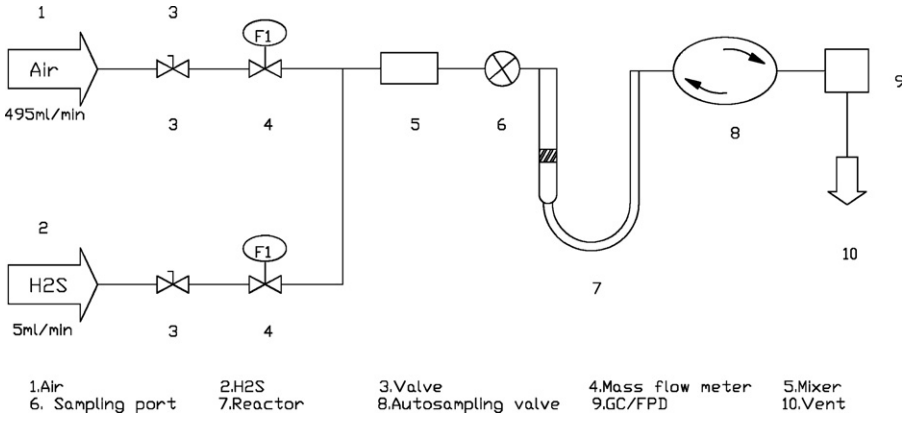

Fig. 1. Scheme of desulphurization experimental system.

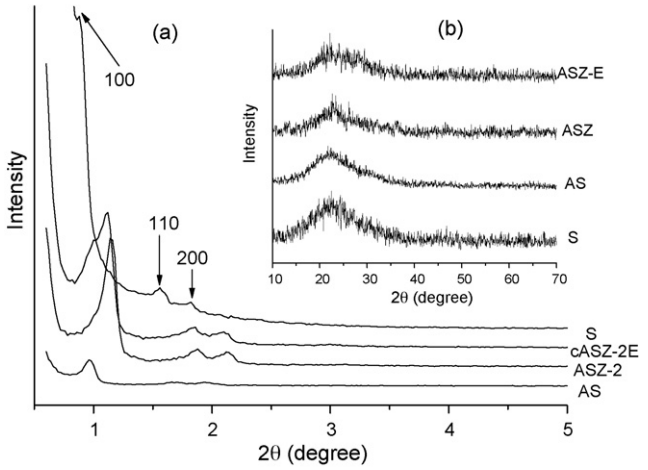

Fig. 2. Small-angle (a) and wide-angle (b) XRD patterns of samples: S, AS, ASZ-2 and ASZ-2E.

Binding energies were measured on PHI 5000C ESCA System (PerkinElmer) with Mg Kα radiation ($h\nu$ = 1253.6 eV) and calibrated by carbon (C_{1s} = 284.6 eV). The data analysis was carried out by using the RBD AugerScan 3.21 software provided by RBD Enterprises.

3. Results and discussions

3.1. Material characterization

The XRD patterns of various materials are shown in Fig. 2. In the small-angle range (Fig. 2a), all samples exhibit the typical pattern of hexagonal structure with a strong diffraction peak near 1° attributed to (1 0 0) and two weak ones indexed to (1 1 0) and (2 0 0). It shows that the introduction of aluminum and immobilization processes does not obviously demolish the mesoscopic order of SBA-15 [16]. Interestingly, the peaks of ASZ shifted towards bigger angles compared with Al–SBA-15, indicating slight shrinkage in the mesoporous framework possibly due to a higher degree of silicate condensation after ZnO modification. In the wide-angle range (Fig. 2b), most samples gave no obvious diffraction peaks. This did not exclude the presence of small clusters of several nanometers in size that do not show X-ray diffraction [23]. Only in ASZ-5 with high Zn content (15.8 wt.%), does the XRD pattern show some peaks of the aggregated ZnO species (not shown). Such results indicate a well-spontaneous dispersion of oxides guest on Al–SBA-15 since a content of 1 wt.% is sufficient to cause sharp peaks in the XRD pattern for crystalline transition metal compounds [24].

The TEM images of various samples are collected in Fig. 3. All images show well-ordered two-dimensional hexagonal (*P6mm*) mesostructure [16]. This confirms that the post-synthesis method is favorable for maintaining the highly ordered mesoporous structure and successfully embedding Al species inside the framework of material. The image of ASZ-2E (Fig. 3d) shows that the particles (the black dot which was tagged by circles) inside the mesopores can be distinguished and dispersed highly on the mesoporous channel of the material. It is possibly the reaction product of the desulphurization reaction. Therefore, it can be inferred that the microwave treatment is an efficient method to scatter guests homogeneously in the hosts.

To infer the impact of ZnO immobilization on the structure of ASZ, the textural properties of ASZ are detected by N_2 adsorption experiments. The N_2 adsorption–desorption isotherms and structural properties are collected in Figs. 4 and 5 and Table 1. The characteristic isotherm of SBA-15 is still preserved with the increase of Zn content. It is consistent with the conclusion obtained by XRD analysis. All isotherms are of type IV (IUPAC classification) and H_1 type hysteresis loop, typical of SBA-15 mesoporous materials [16]. It is noteworthy that an H_1 type hysteresis indicates the presence of open channels for ASZ. This is important for catalytic applications, which requires an effective diffusion of the reactants through the porous materials. The hysteresis loop with a two-step desorption branch described by Janssen et al. [25] for plugged SBA-15 material is observed, indicating mesopore blockage after ZnO immobilization. In addition, all isotherms show a steep capillary condensation step at a relative pressure of 0.6, indicating a narrow mesopore size distribution. The *t*-plot of material does not pass the zero of the axis, suggesting that the material has micropore [26]. Those of ASZ samples are closer to the zero of the axis with the increase of Zn content (not shown). It can be therefore concluded that immobilization process of high Zn content results in the decrease of micropore. The standpoint can be confirmed from the data in Table 1. The textural properties, such as specific BET surface area, micropore area, micropore volume, and total pore volume for ASZ are found to be dependent on the Zn addition. It is remarkable that the micropore surface area and micropore volume of ASZ-2 is almost the same as ASZ-1, but those of other ASZ (ASZ-3, 4 and 5) decrease quickly with the increase of the Zn content. It is possible that ZnO nanoparticles also entered the micropores on the wall of AS due to the microwave treatment, except the mesopores and the external surface of material. Therefore, the Zn content plays a key role in controlling the porosity of the material in this case.

Table 1
Structural property of various samples determined by N_2-adsorption

Sample	BET surface area (m^2/g)	Micropore area (m^2/g)	Micropore volume (cm^3/g)	Total pore volume (cm^3/g)	BJH desorption average pore diameter (nm)
S	686.7	234.6	0.10	1.64	8.2
AS	453.6	57.1	0.02	0.64	5.4
ASZ-1	445.8	40.6	0.01	0.65	5.1
ASZ-2	434.0	39.8	0.01	0.69	5.9
ASZ-2E	427.0	49.1	0.02	0.72	6.3
ASZ-3	322.7	25.4	0.01	0.56	5.8
ASZ-4	327.4	19.7	0.01	0.55	5.8
ASZ-5	222.3	15.8	0.01	0.45	6.6

The pore size distribution (PSD) curves in Fig. 5b for ASZ show narrow pore size distribution with an average pore size of about 60 Å. Additional mesopores with an average size in the range of 30–40 Å were also noticed in all samples. The results validate that Al–SBA-15 supported ZnO consists of mesopores of size smaller than 3.4 nm as well as micropores in the walls [27,28], besides the mesopore.

FTIR spectra patterns (in Fig. 6) show that those absorbed peaks characteristic of SBA-15 due to Si–O–Si backbone vibrations around 1237, 1132, 1084, 800, and 460 cm^{-1} associated with the formation of a condensed silica network remain essentially, even after alumination, ZnO modification processes. But weak peaks associated with noncondensed Si–OH groups in 964 cm^{-1} [29,30] were also present. The fairly sharp peak at 460 cm^{-1} is also due to ZnO [31], indicating the dispersion homogeneously of ZnO in ASZ. The 800 cm^{-1} peak cannot be resolved due to its overlap with the absorbed peaks of Si–O–Al bending vibrations [32]. The broad peak at 3455 cm^{-1} can be assigned to the O–H stretching vibrations of the hydrogen-bonded silanol groups [33–35] and adsorbed water molecules. There is an abundance of silanol groups present in the parent Al–SBA-15 silica that essentially lines the interior surface of

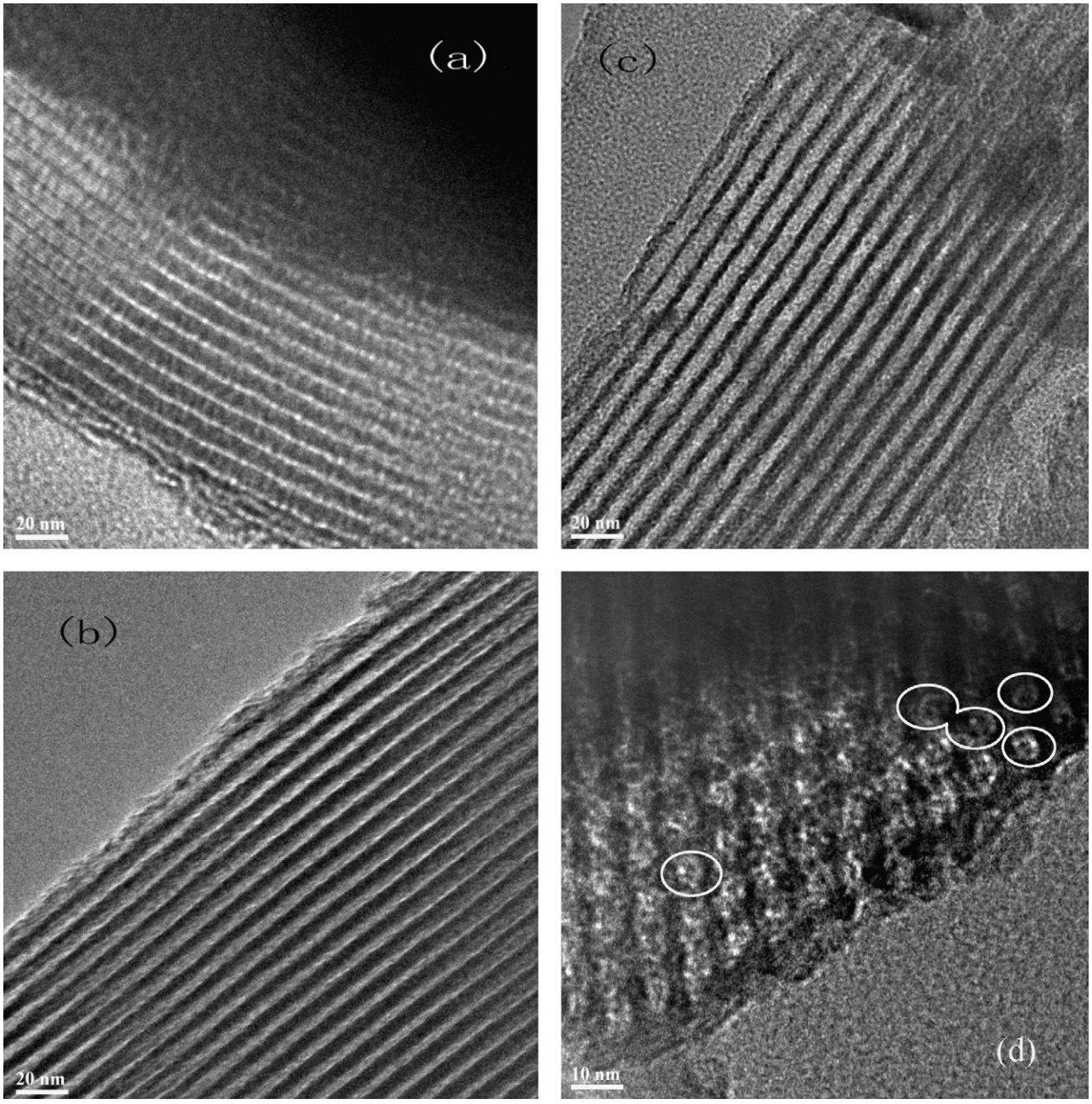

Fig. 3. TEM images of (a) S, (b) AS, (c) ASZ-2 and (d) ASZ-2E.

the mesoporous channels. The silanol groups on the internal surface of the parent Al–SBA-15 silica are the sites for incorporation of ZnO nanoparticle and are consumed, i.e., ZnO nanoparticles are chemically bonded on the internal surface of the Al–SBA-15 material.

3.2. Desulphurization activity

The performance of ASZ samples and neat ZnO for H_2S capture was tested using the measurement procedures described before. The results of elemental analysis and the H_2S breakthrough capacities and the pH value of initial and exhausted materials for ASZ and neat ZnO are listed in Table 2. The H_2S breakthrough curves are shown in Fig. 7. The Al content decreased with the increase of Zn content for ASZ samples. At the same time, the content of sodium increased markedly introduced during the preparation process. It indicates that the substitution of Al species in the framework occurred during immobilization process. As mentioned previously [36,37], this procedure leads to a partial elimination of the substituted trivalent element. Results also showed that the pre-breakthrough H_2S levels in the outlet gas remained far below 0.1 ppm. No H_2S removal was observed for zinc-free Al–SBA-15. The activity of neat ZnO nanoparticles is about 46.0 mg S/g material. The highest H_2S breakthrough capacity, 103.2 mg S/g adsorbent, was observed ASZ-2. It is slightly lower than that of Centaur (104.0 mg S/g adsorbent) [38,39], one of the best commercial catalytic carbons on the market. It indicates that Al–SBA-15 supported ZnO has higher removal capacity than neat ZnO nanoparticles and is efficient for H_2S capture from the gaseous streams. A slight decrease in pH for

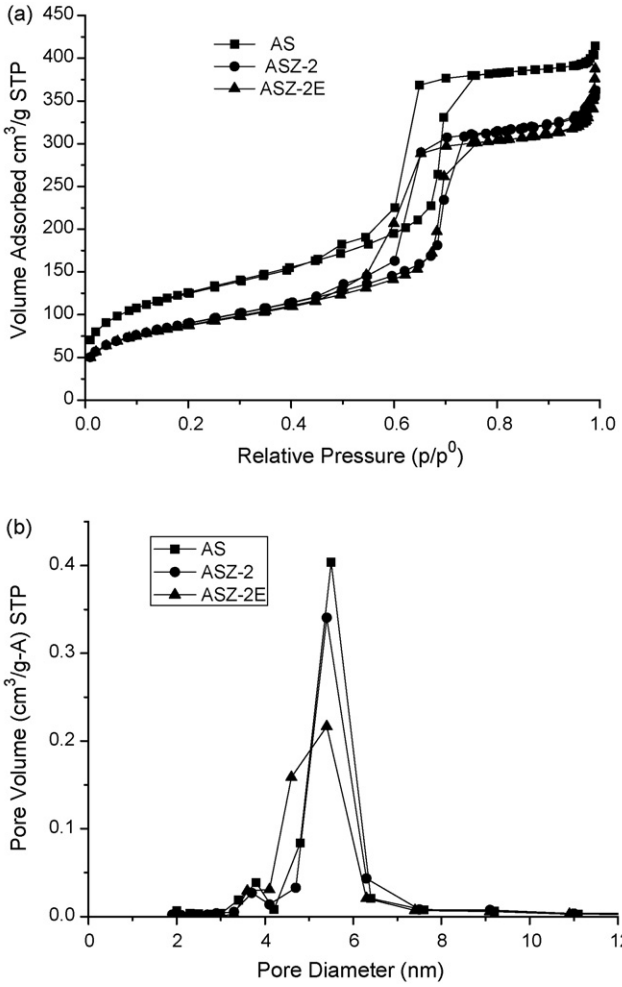

Fig. 4. Nitrogen adsorption–desorption isotherms (a) and pore size distribution (b) of AS, ASZ-2 and ASZ-2E.

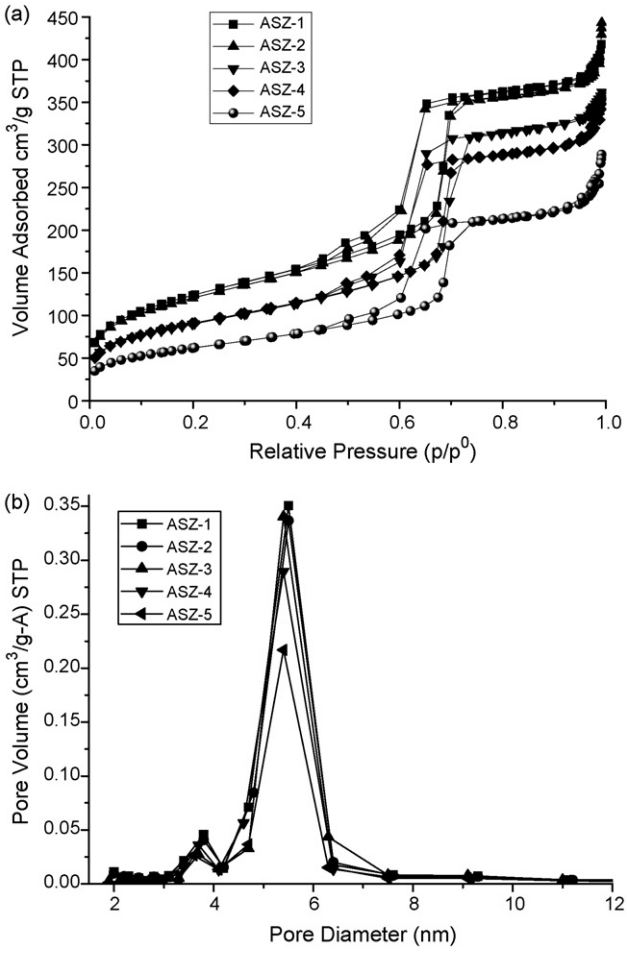

Fig. 5. Nitrogen adsorption–desorption isotherms (a) and pore size distribution (b) of ASZ.

ASZ-E was observed, possibly caused by the deposition of reaction products.

To understand the role of ZnO chemistry, the dependence of the Zn content and the breakthrough capacity of materials were analyzed. The breakthrough capacity of materials initially increased and then decreased with the increase of Zn content. A significant enhancement in the desulphurization performance was found over ASZ-2. It is believed that Zn^{2+} serves as extra framework charge compensation cation during the substitution process of Al^{3+} in the silica framework [40]. It introduces novel functionality into the mesoporous silicate. Low Zn content improves H_2S uptake capacity. However, excessive additive content is detrimental to desulphurization performance. In an effort to identify the surface features of ASZ that do govern their desulphurization performances, the relationship between H_2S breakthrough capacity and structural properties was studied. The hysteresis loop with a two-step desorption branch for ASZ-2E indicated mesopore blockage (Fig. 4a), possibly due to mesopore filling of desulphurization products. Therefore, mesopore is the active site for H_2S capture. Adding 2.1% of Zn content in ASZ-2 but 4.1% in ASZ-3 resulted in 24% decrease in the surface area and microporosity. Therefore, surface area and micropores correlate with the desulphurization performance over ASZ. About 29% and 5.2% increase in the microporosity and mesoporosity which is in terms of the ratio of the micro/mesopore and the total pore volume was observed during H_2S capture process, respectively. So it can be inferred that both mesopore and micropore are active sites for desulphurization activity, especially micropore.

Table 2
Element analysis and H_2S breakthrough capacities of ASZ samples and neat ZnO

Sample	Zn[a] (wt.%)	Al[a] (wt.%)	Na[a] (wt.%)	H_2S breakthrough capacity (mg S/g sorbent)	pH (initial)	pH (exhausted)
ASZ-1	0.8	1.4	0.3	48.5	5.6	5.5
ASZ-2	2.1	1.0	0.5	103.2	7.0	6.1
ASZ-3	4.8	0.8	1.2	77.9	8.1	8.1
ASZ-4	13.0	0.6	2.7	47.4	8.7	8.6
ASZ-5	15.8	0.5	3.4	29.6	9.3	9.1
ZnO	76.1	–	–	46.0	–	–

[a] Determined by ICP.

3.3. Material characterization after desulphurization reaction

The whole spectra of all the elements for ASZ-2 and ASZ-2E are shown in Fig. 8. The binding energies (BE) of some characteristic core levels are collected in Table 3. XPS analysis of ASZ-2 showed a single $Zn_{2p3/2}$ peak at 1022.5 eV corresponding to ZnO. The BE of $Zn_{2p3/2}$ for ASZ-2E shifts to a lower region at 1021.8 eV assigned to ZnS. To obtain further reaction information, more XPS analysis of other elements was also conducted on ASZ-2E and ZnO-E to identify desulphurization reactions. The $S_{2p3/2}$ peak at 162 eV for

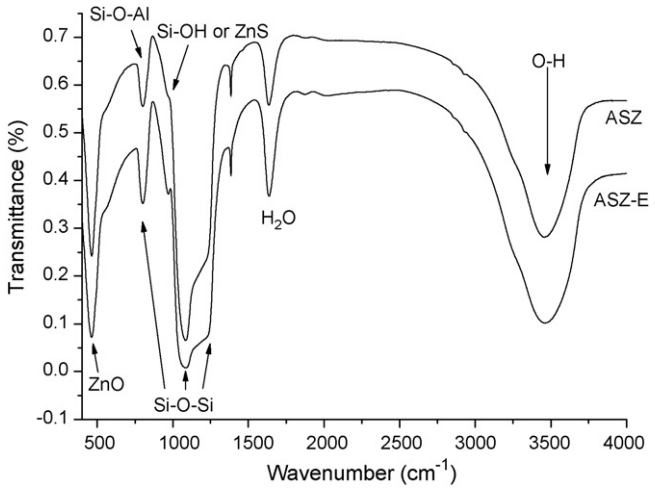

Fig. 6. FTIR spectra of the ASZ-2 before and after H_2S desulphurization test.

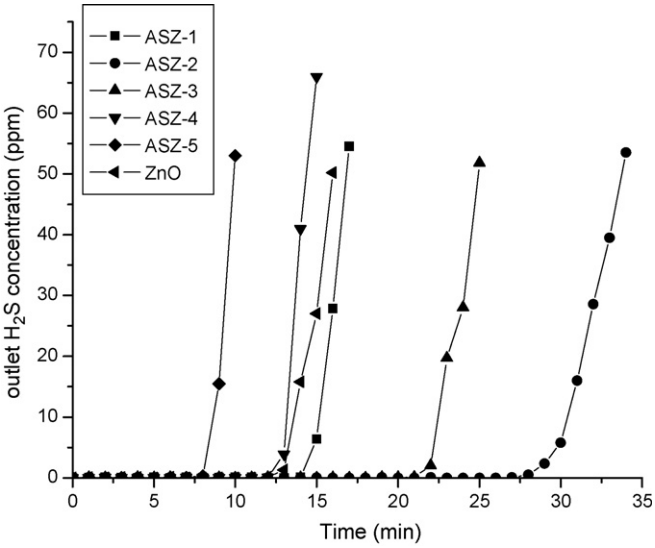

Fig. 7. H_2S breakthrough curves for ASZ samples and neat ZnO. Operation conditions: 1 atm, 298 K, inlet gas mixture: 0.1% H_2S, balance of air, 500 ml/min, mass of adsorbent from ASZ-1 to ASZ-5: 99, 98, 103, 104 and 108 mg; the average density of the beds: 95 mg/cm^3.

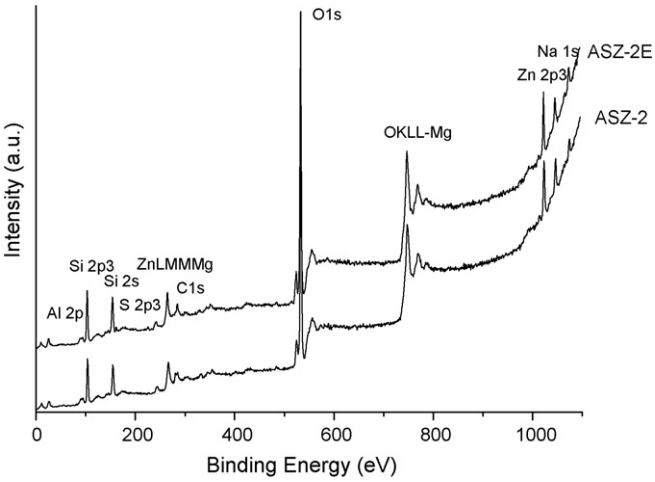

Fig. 8. XPS spectra of the whole spectra for ASZ-2 and ASZ-2E.

Table 3
XPS binding energy (eV) of ASZ samples and neat ZnO before and after desulphurization test

Sample	$Si_{2p3/2}$	$Zn_{2p3/2}$	$S_{2p3/2}$	Al_{2p}
ASZ-2	103.5	1022.5	–	74.6
	SiO_2	ZnO	–	Al_2O_3
ASZ-2E	103.3	1021.8	162	74.9
	SiO_2	ZnS	ZnS	AlO_x
ZnO	–	1022.1	–	–
	–	ZnO	–	–
ZnO-E	–	1022.0	161.6	–
	–	ZnO	ZnS	–

ASZ-2E is attributed to ZnS. Thus, the reaction product over Al–SBA-15 supported ZnO is ZnS. The conclusion is validated by XRD results. The crystalline size of ASZ-2E is much bigger than ASZ-2, indicating that desulphurization product might be ZnS. Since the molar volume ratio of ZnS and ZnO is 1.6 [41]. The FTIR spectra patterns for ASZ-E (Fig. 6) validated that the peak at 968 cm^{-1} for ASZ-2E strengthened remarkably. That indicates that ZnS possibly formed after the desulphurization test overlapped the peak of the noncondensed Si–OH groups at this region [42].

From the results of the FTIR, XRD and XPS, it can be well assessed that the H_2S capture over Al–SBA-15 supported ZnO at room temperature occurs due to gas–solid reactions in a thin hydrated lattice of metal oxides. This process leads to the formation of sulphide: $ZnO + H_2S \rightarrow ZnS + H_2O$.

XPS analysis of neat ZnO showed $Zn_{2p3/2}$ peak at 1022.1 eV corresponding to ZnO. The $S_{2p3/2}$ peak at 161.6 eV for ZnO-E is attributed to ZnS, indicating the same process of the H_2S capture over neat ZnO as that over Al–SBA-15 supported ZnO.

Interestingly, adsorbed sulphur atoms per zinc atom (S/Zn) can be evaluated from the results in Table 2. The values of S/Zn for ASZ-1, -2, -3, -4 and -5 were 12.7, 10.3, 3.9, 0.7 and 0.4, respectively. Therefore, it is obvious that there is another cause of the excess sulphur atoms adsorbed at the same time except the gas–solid reactions. Pore structure parameters of various samples determined by XRD and nitrogen adsorption are shown in Table 4. Physical adsorption of hydrogen sulphide in micropores of activated carbon is negligible since the reactions mentioned occur at room temperature and atmospheric pressure [43]. However, the introduction of Al in the siliceous framework changes the composition of the inorganic walls and results in the formation of Brönsted acidity and ion-exchange sites, similar as observed in zeolites [44]. It is likely that sodium present inside the pore of ZnO/Al–SBA-15 react with physically adsorbed H_2S in adsorbed water. It probably results in the formation of water-soluble sulphur species. Combining with the discussion for active sites of desulphurization activity mentioned above, it can be inferred that micropore in ASZ possibly contributes to a considerable breakthrough capacity. This conclusion can be validated from the change of pore structure parameters of samples determined by XRD and nitrogen adsorption (shown in Table 4). The pore size increased from 5.9 to 6.3 nm

Table 4
Pore structure parameters of various samples determined by XRD and nitrogen adsorption

Sample	$d_{1\,0\,0}$ (nm)	a_0 (nm)	W_{BJH} (nm)	T_W (nm)
S	10.0	11.5	8.2	5.5
AS	9.2	10.6	5.4	5.2
ASZ-2	8.0	9.2	5.9	3.3
ASZ-2E	8.2	9.5	6.3	3.2

d is spacing and primary mesopore volume, a_0 is the XRD unit cell parameter, W_{BJH} is pore size determined from BJH desorption data and T_W is wall thickness.

and the pore wall thickness slightly decreased from 3.3 to 3.2 nm after desulphurization test. It possibly indicates that the loss of sodium on the surface of the mesoporous channel introduced during the preparation process.

In addition, more information was obtained from the results of characterization techniques. The FTIR spectra patterns for ASZ-E (Fig. 6) show that desulphurization reaction did not demolish the framework since the backbone vibrations remained essentially unchanged. In the small-angle range (Fig. 2a), the diffraction peaks corresponding to *P6mm* hexagonal symmetry for ASZ-2E show that desulphurization processes do not affect the mesoscopic order of ASZ-2. This is consistent with the images observed by TEM analysis.

4. Conclusions

Al–SBA-15 supported ZnO, synthesized by the post-synthesis and immobilization method, successfully embeds Al inside the framework of SBA-15 and maintains highly ordered 2D hexagonal mesoporous structures. ZnO nanoparticles dispersed well on the wall, the surface and in the channel of Al–SBA-15. They anchored both in the micropore and the mesopore in virtue of the microwave treatment during the immobilization process.

A superior ability to remove sulphur down to 0.1 ppm from the gaseous streams containing 0.1% H_2S was observed. The material with 2.1 wt.% Zn loading showed the highest sulphur trapping capacity (103.2 mg S/g sorbent). Surface chemistry and pore structure of the mesoporous material might be the limiting factors on H_2S breakthrough capacity in this case. Both micropores and mesopores are active sites for H_2S capture, especially micropore.

The mesostructure material prepared in this study exhibits a promising catalytic reactivity for gas cleaning at room temperature. It broadens the application of mesoporous material to separation and purification of gaseous streams.

References

[1] L. Mercier, T.J. Pinnavaia, Chem. Mater. 12 (2000) 188.
[2] C.T. Kresge, M.E. Leonowicz, W.J. Roth, J.C. Vartuli, J.S. Beck, Nature 359 (1992) 710.
[3] A. Stein, Adv. Mater. 15 (2003) 763.
[4] I. Rodriguez, S. Iborra, A. Corma, F. Rey, J.L. Jordá, Chem. Commun. 7 (1999) 593.
[5] J.S. Beck, J.C. Vartuli, W.J. Roth, M.E. Leonowicz, C.T. Kresge, K.D. Schmitt, C.T.-W. Chu, D.H. Olson, E.W. Sheppard, S.B. McCullen, J.B. Higgins, J.L. Schlenker, J. Am. Chem. Soc. 114 (1992) 10834.
[6] S. Dai, M.C. Burleigh, Y. Shin, C.C. Morrow, C.E. Barnes, Z. Xue, Angew. Chem. Int. Ed. 38 (1999) 1235.
[7] H. Yoshitake, T. Yokoi, T. Tatsumi, Chem. Mater. 15 (2003) 1713.
[8] V.S.-Y. Lin, C.-Y. Lai, J.H. Huang, S.-A. Song, S. Xu, J. Am. Chem. Soc. 123 (2001) 11510.
[9] A. Corma, Chem. Rev. 97 (1997) 2373.
[10] L. Zhang, T. Sun, J.Y. Ying, Chem. Commun. 12 (1999) 1103.
[11] D. Das, J.-F. Lee, S. Cheng, Chem. Commun. 21 (2001) 2178.
[12] X. Feng, G.E. Fryxell, L.-Q. Wang, A.Y. Kim, J. Liu, K.M. Kemner, Science 276 (1997) 923.
[13] J. Brown, L. Mercier, T.J. Pinnavaia, Chem. Commun. 1 (1999) 69.
[14] V. Kuchi, A.M. Oliver, M.N. Paddon-Row, R.F. Howe, Chem. Commun. 12 (1999) 1149.
[15] S. Baskaran, J. Liu, K. Domansky, N. Kohler, X. Li, C. Coyle, G.E. Fryxell, S. Thevuthasan, R.E. Williford, Adv. Mater. 12 (2000) 291–294.
[16] D.Y. Zhao, J.L. Feng, Q.S. Huo, N. Melosh, G.H. Fredrickson, B.F. Chmelka, G.D. Stucky, Science 279 (1998) 548.
[17] Y. Ueno, A. Tate, O. Niwa, H.-S. Zhou, T. Yamada, I. Honma, Chem. Commun. 6 (2004) 746.
[18] Y. Li, Z.C. Feng, H.C. Xin, F.T. Fan, J. Zhang, P.C.M.M. Magusin, E.J.M. Hensen, R.A. van Santen, Q.H. Yang, C. Li, J. Phys. Chem. B 110 (2006) 26114.
[19] D. Stirling, The Sulfur Problem: Cleaning Up Industrial Feedstocks, Royal Society of Chemistry, Cambridge, 2000, p. 33.
[20] W.G. Feng, E. Borguet, R.D. Vidic, Carbon 44 (2006) 2990–2997.
[21] E.P. Barret, L.G. Joyner, P.P. Halenda, J. Am. Chem. Soc. 73 (1951) 373.
[22] K.S.W. Sing, D.H. Everett, R.A.W. Haul, L. Moscou, R.A. Pierotti, J. Rouquerol, T. Siemieniewska, Pure Appl. Chem. 57 (4) (1985) 603.
[23] A. Auroux, A. Gervasini, C. Guimon, J. Phys. Chem. B 103 (1999) 7195.
[24] Y.C. Xie, Y.Q. Tang, Adv. Catal. 37 (1990) 1.
[25] A.H. Janssen, C.-M. Yang, Y. Wang, F. Schüth, A.J. Koster, K.P. de Jong, J. Phys. Chem. B 107 (2003) 10552.
[26] Y. Han, S. Wu, Y.Y. Sun, D.S. Li, F.-S. Xiao, J. Liu, X.Z. Zhang, Chem. Mater. 14 (2002) 1144.
[27] M. Kruk, M. Jaroniec, T.-W. Kim, R. Ryoo, Chem. Mater. 15 (2003) 2815.
[28] M. Kruk, M. Jaroniec, Chem. Mater. 12 (2000) 1961.
[29] M. Llusar, G. Monrós, C. Roux, J.L. Pozzo, C. Sanchez, J. Mater. Chem. 13 (2003) 2505.
[30] A. Lapkin, B. Bozkaya, T. Mays, L. Borello, K. Edler, B. Crittenden, Catal. Today 81 (2003) 611.
[31] R.A. Nyquist, R.O. Kagel, Infrared Spectra of Inorganic Compounds, Academic Press, New York, 1971.
[32] M.T. Janicke, C.C. Landry, S.C. Christiansen, S. Birtalan, G.D. Stucky, B.F. Chmelka, Chem. Mater. 11 (1999) 1342.
[33] P.T. Tanev, L.T. Vlaev, J. Colloid Interface Sci. 160 (1993) 110.
[34] H. Kosslick, H. Landmesser, R. Fricke, J. Chem. Soc., Faraday Trans. 93 (1997) 1849.
[35] S.-C. Shen, S. Kawi, J. Phys. Chem. B 103 (1999) 8870.
[36] D.T. On, P.N. Joshi, S. Kaliaguine, J. Phys. Chem. 100 (1996) 6743.
[37] K. Okumura, K. Nishigaki, M. Niwa, Micropor. Mesopor. Mater. 44–45 (2001) 509.
[38] R.A. Hayden, U.S. Patent 5 (1995) 444, 031.
[39] T.M. Matviya, R.A. Hayden, U.S. Patent 5 (1994) 356, 849.
[40] A. Taguchi, F. Schüth, Ordered mesoporous materials in catalysis, Micropor. Mesopor. Mater. 77 (2005) 1.
[41] S.C. Christoforou, E.A. Efthimiadis, I.A. Vasalos, Ind. Eng. Chem. Res. 34 (1995) 83.
[42] K.D.O. Jackson, A guide to identifying common inorganic fillers and activators using vibrational spectroscopy, Int. J. Vib. Spectrosc. 2 (1998) Edition 3.
[43] F. Adib, A. Bagreev, T.J. Bandosz, J. Colloid Interface Sci. 216 (2) (1999) 360.
[44] T.J. Bandosz, Carbon 37 (1999) 483.